International Journal of Heat and Mass Transfer 101 (2016) 341–353

Contents lists available at ScienceDirect

International Journal of Heat and Mass Transfer

journal homepage: www.elsevier.com/locate/ijhmt

Porous-wall microchannels generate high frequency "eye-blinking" interface oscillation, yielding ultra-stable wall temperatures

Jinliang Xu *, Xiongjiang Yu, Wu Jin

The Beijing Key Laboratory of Multiphase Flow and Heat Transfer for Low Grade Energy Utilization, North China Electric Power University, Beijing 102206, PR China

ARTICLE INFO

Article history:
Received 6 March 2016
Received in revised form 8 May 2016
Accepted 9 May 2016

Keywords:
Microchannel
Flow instability
Heat transfer
Boiling/evaporating
Vapor–liquid interface

ABSTRACT

The proposed gradient–porous-wall microchannels consist of bare channels and pin–fin array regions, fabricated by MEMS (microelectricalmechanicalsystem) technique. Boiling experiments were performed with acetone as the working fluid. Ultra-stable wall temperatures are achieved with oscillation amplitudes in the range of 0.02–0.18 °C. Bubble nucleation is found to happen in the porous wall. The generated vapor flows towards bare channels due to surface tension driving flow. The vapor ejection direction is periodically switched between neighboring channels, called the "bubble emission switch". The bubble confinement ratio is newly defined. Bubbles become fat and slim in bare channels to generate high frequency "eye-blinking oscillation". Bubble confinement ratios display sine function, and out-of-phase characteristic between neighboring channels. We confirm the "eye-blinking" oscillation as a density wave oscillation, propagating in the channel width direction. Because the porous-wall width is much smaller than the channel length, the "eye-blinking" frequencies are 10–100 times higher than that of the axially propagated density wave oscillation. The "integration parameter model" establishes the connection between "eye-blinking" oscillation and wall temperatures. The convective heat transfer intensity in bare channels is assumed to follow the bubble confinement ratio variation. The wall temperature oscillation amplitude is inversely proportional to the "eye-blinking" frequency. The phase angle between bubble confinement ratios and wall temperatures are $3\pi/2$, being the negative feedback mechanism to inhibit wall temperature oscillations. The porous-wall microchannels open a new way to eliminate flow instabilities for heat exchangers and thermal energy systems.

1. Introduction

Historically, Ledinegg [1] is the pioneer work of two-phase flow instability. From 1960s to 1980s, the development of high power density boilers and pressurized water reactors attracted many researchers to investigate two-phase flow instabilities in tubes, heat exchangers and energy systems. It is not until late 1980s that the main instability mechanisms were understood. Now, the abundant articles or books recorded various phenomena and mechanisms. The detailed literature survey is beyond the scope of the present paper, but can be found in review articles [2,3].

The dynamic flow instability is more complicated compared with the static instability. Three typical types of flow instabilities may occur: pressure drop oscillation (PDO), density wave oscillation (DWO) and thermal oscillation (TO). They may be coupled with each other. PDO occurs if there is a large compressible volume upstream of the boiling channels. The pressure drop oscillation was analyzed by Stenning [4], Stenning and Veziroglu [5], etc. The increase of inlet flow resistance is an effective way to eliminate the pressure drop oscillation, with the penalty of increased pumping power. The density wave oscillation is widely studied in large size channels. It is related to the dynamic variation of the two-phase mixture densities. It is influenced by various factors such as flow patterns, void fractions, heat transfer and pressure drops. Oscillation cycle period relies on the propagation time of the disturbances of fluid particles, which is about 1.5–2 times of the fluid residence time in the channel [6].

Microchannel heat sink was proposed in 1980s for high power density electronic cooling, in which boiling/evaporation heat transfer in microchannels offers advantages compared with the single-phase heat transfer. However, experimental observations in the last decade showed apparent oscillations of pressure drops, flow rates and wall temperatures. Wu and Cheng [7] investigated boiling instabilities in silicon microchannels. They found large amplitude/long period oscillations. The oscillation cycle periods can be up to 10–100 s and the wall temperatures are oscillating with the amplitude of several tens of degrees. Xu et al. [8] measured

* Corresponding author. Tel./fax: +86 10 61772613.
E-mail address: xjl@ncepu.edu.cn (J. Xu).

http://dx.doi.org/10.1016/j.ijheatmasstransfer.2016.05.039
0017-9310/

Nomenclature

A	vapor–liquid interface area per unit flow length (m^2)
A_{film}	thin film heating area (m^2)
A_c	effective cross section area of the microchannel (m^2)
Bi	*Biot* number
Co	bubble confinement number
C_p	specific heat (J/kg K)
D	hydraulic diameter (m)
f	frequency (Hz)
G	mass flux (kg/m^2 s)
g	gravity force (m/s^2)
h	specific enthalpy (J/K)
h_{fg}	latent heat of evaporation (J/K)
i	number of bare channel
K	non-dimensional K number
L	bubble slug length (m)
l	length (m)
l_c	capillary length
l_{mc}	microchannel length (m)
l_{unit}	length of unit (m)
m	mass flow rate (kg/s); mass (kg)
m_e	evaporation rate (kg/s)
n	number of samples
n_p	number of pixels
P	pressure (Pa)
ΔP	pressure drop across the microchannel (Pa)
Δp	pressure drop (Pa)
Q	effective heating power (W)
Q_h	heat source (W)
Q_t	heat power (W)
q	effective heat flux (W/m^2)
R	gas constant for vapor (J/mol K)
R_s	standard resistance (Ω)
S	slip ratio
S_n	non-dimensional oscillation amplitude
S_{tp}	ratio of vapor velocity to liquid velocity
T	temperature (°C)
ΔT_{sub}	inlet liquid subcooling temperature (°C)
$T_{X,Y}(t)$	wall temperature at the location (X,Y) at time t (°C)
$\bar{T}_{X,Y}$	time averaged temperature at (X,Y) (°C)
V_1	voltage on film heater (V)
V_2	voltage on standard resistance and film heater (V)
V_{vacuum}	vacuum volume in the microchannel region (m^3)
v_r	radial velocity
W	bare channel width (m)
W_{porous}	porous wall width (m)
w	bubble width (m)
w_s	characteristic sizes for smaller space (m)
w_l	characteristic sizes for larger space (m)
X	length along flow direction (mm)
x	vapor mass quality
Y	length along width direction (mm)

Greek symbols

α	void fraction; convective heat transfer coefficient (W/m^2 K)
αA	film convective heat transfer intensity (W/K)
δ_c	etched channel depth (m)
η	bubble confinement ratio
μ	dynamic viscosity (kg/m s)
$\Delta\rho$	density difference between vapor and liquid (kg/m^3)
ρ	density (kg/m^3)
σ	surface tension force (N/m)
$\sigma(X,Y)$	standard deviation at position (X,Y)
τ	fluid residence time (s)
φ	thermal efficiency

Subscripts

ave	average
eff	effective
f	liquid
g	vapor
i	number of channel
in	inlet
m	average
max	maximum
out	outlet
r	residence
s	solid
sat	saturated
sp	liquid phase
w	wall
1	upstream; small space
2	downstream; large space

onset of flow instability (OFI) (static flow instability) and dynamic flow instability using 26 rectangular microchannels each with a width of 300 μm and a depth of 800 μm, using deionized water as the working fluid. The onset of flow instabilities was identified as occurring at the outlet temperature of 93–96 °C, which is several degrees lower than the saturation temperature corresponding to the exit pressure. In conditions that the mass flux is lower than that at the OFI condition, three types of flow instability were identified: large amplitude/long period oscillation, small amplitude/short period oscillation, and thermal oscillation. The reported cycle periods are also very long. Other studies related to boiling instabilities can be found in Refs. [9–15].

In order to understand instability mechanisms in microchannels, Lyu et al. [16] used the wavelet decomposition method to remove the nose signal from the mother signal and decouple the oscillation signal at different timescales. Silicon microchannels were used and water was the working fluid. The bottom wall temperatures were measured by a high spatial-time resolution IR (infrared radiation) image system, having a temperature sensitivity of 0.02 °C. The recording rate was 500 simples per second. All the parameters (pressures, flow rates, temperatures, and flow patterns) are synchronously measured. By decomposition of the signal at different timescales, it is found that the so-called large amplitude/long period oscillation is the pressure drop oscillation (~10 s cycle period), while the density wave oscillation displays the cycle period of ~10 ms (corresponding to the frequency of ~100 Hz). The mechanisms of the two oscillations are similar to those happened in large size channels. However, the varied liquid film evaporation induced oscillation is specific to microchannels.

Even though many studies are reported in the literature, flow instabilities in microchannels are not fully understood. The flow instabilities induce wall temperature oscillations to cause the varied thermal stress across the microfluidic chip. Many engineering applications need to suppress the temperature oscillations significantly. The wall temperatures should be stable enough for precise thermal management [17–19]. Various methods such as the introduction of pressure resistance element at the microchannel upstream [20], artificial nucleation cavities on channel walls [21] and injection of seed bubbles in microchannels [22] were used to eliminate the flow instabilities.

When the channel size is decreased, the bubble expansion can only be performed along the flow direction, yielding the bubble confinement effect. The microchannels reduce the 3D effect. Besides, the multi-channels can have many solutions of flow rates [23]. The bubble confinement and multi-channel effects are coupled with each other, making the problem more complicated.

This paper introduced porous-wall microchannels. The porous walls are pin–fins with specific fin gaps here. Owning to such specific fin gaps, mass exchange between neighboring channels is possible at any axial location when the fluid flows in bare channels. What is more, such porous walls have many corners that can be nucleation sites, enabling nucleation heat transfer happening within porous walls. The generated vapor automatically flows towards the bare channel driven by the surface tension force. The liquid film evaporation heat transfer appears in bare channels. When the pressure is slightly increased due to the vapor expansion, the liquid can be expelled into its neighboring bare channel. The negative feedback is established between vapor expansion and wall temperatures. Thus, pressure in such a bare channel returns to be reduced, creating the "eye-blinking" motion of the vapor–liquid interface. This process can be characterized based on the liquid traveling time across the porous wall. Because the porous wall width is significantly smaller compared with the channel length, the "eye-blinking" motion is self-sustained at high frequency. We demonstrate that the oscillation amplitude of wall temperatures is significantly decreased at high frequencies of the "eye-blinking" motion. Thus, an ultra-stable wall temperatures are reached. The porous-wall-microchannels open a new way to suppress the thermal oscillations, involving many engineering microfluidic applications.

2. Bubble confinement in microchannels

Flow instability mechanisms in large channels, may also occur in small channels, but some differences may exist. The bulk fluid related phenomenon is important in large channels, but the wall effect plays an important role in small channels. The 3D effects are apparently decreased in narrow channels. The capillary length is defined as

$$l_c = \sqrt{\frac{\sigma}{g\Delta\rho}} \tag{1}$$

where σ, g and $\Delta\rho$ are the surface tension force, gravity force and density difference between vapor and liquid, respectively. The bubble confinement number (Co) is defined as the ratio of the capillary length l_c to the channel hydraulic diameter D: $Co = l_c/D$. For $Co > 1$, the capillary effect is important for two-phase flow. The growing bubble may occupy the cross section of the channel before it detaches from the wall. The isolated bubbles seldom appears. They only appear at the onset of boiling in a short channel length. The elongated bubble flow is the dominant flow pattern in small channels.

When dealing with boiling in microchannels, Kandlikar [24] considered the balance between the evaporation momentum force related to the surface tension force. The non-dimensional K number was defined as

$$K = \left[\frac{q}{Gh_{fg}}\right]^2 \frac{D}{\rho_g \sigma} \tag{2}$$

where q is the heat flux, G is the mass flux, h_{fg} is the latent heat of evaporation, and ρ_g is the vapor density. The $K > 1$ indicates that the evaporation momentum force is over the surface tension force to cause the future bubble expansion, until the channel cross section is occupied by the bubble.

The following paragraph discusses how the bubble confinement cause the channel blockage and the multi-channel effect. The channel blockage and uneven flow distribution are the major mechanisms to cause flow instability in microchannels. Fig. 1a shows a bubble slug in a rectangular microchannel. Due to the bubble confinement, liquid flow is forced to flow through channel corner regions. The liquid flow can be treated as Poiseuille flow and the pressure drop can be written as [25]:

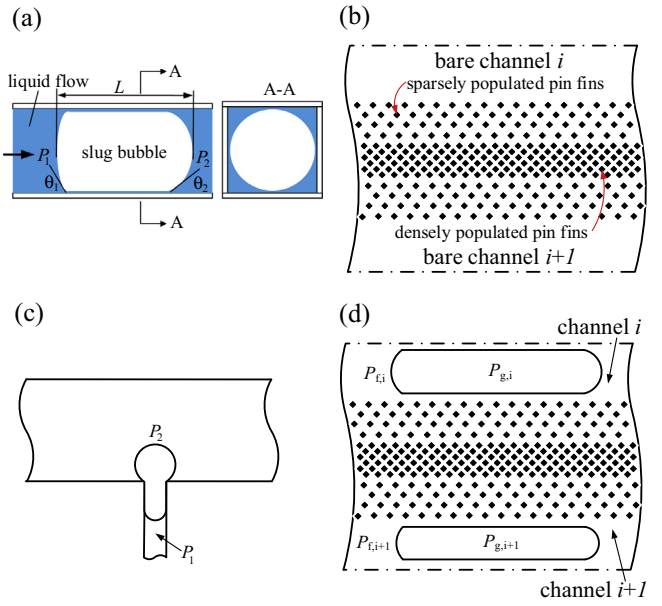

Fig. 1. Bubble dynamics in microchannels ((a) for bubble confinement in conventional microchannels, (b) for gradient–porous-wall microchannel design, (c) for surface tension force driven bubble flow from a small hole to a large space, (d) for pressure analysis in two neighboring bare channels across the porous wall).

$$\Delta p = P_1 - P_2 = \frac{128\mu_f L m_f}{\pi D_{eff}^4} \tag{3}$$

where P_1 and P_2 are the upstream and downstream pressures, respectively, μ_f, L and m_f are the liquid viscosity, bubble slug length and mass flow rate of the liquid, respectively, and D_{eff} is the effective dynamic diameter of the liquid flow, represented by the blue corner region of the channel (see Fig. 1a).

When the bubble slug is sufficiently long, the pressure drop required to propel the bubble is quite high when compared with that of large channels. This is because most of the channel cross section is occupied by vapor phase, liquid only flows in channel corner region. When the external pumping pressure is limited, liquid flow rate in a long bubble channel is decreased. This causes the extra liquid flow rate flows through other channels. This effect causes significantly uneven flow distribution between different channels. This analysis is consistent with the experimental observations such as Peles et al. [26].

In summary, bubble confinement yields elongated bubble in microchannels, liquid flow is difficult to be established, or the boiling/evaporation flow needs a higher pumping power. Eq. (3) tells us that partial channel blockage is possible and strong multi-channel effect occurs. These phenomena are caused by the microchannel geometry: mass exchange only occurs at the upstream plenum of microchannels. The pressure expansion in a specific microchannel can only be released along the flow direction, due to the solid walls without holes.

3. Porous-wall microchannels concept

The porous walls are introduced to separate different channels (see Fig. 1b for the top view). The porous wall can be pin fins,

but can have different pore sizes. For example, the pin fins are densely and sparsely populated in the center region and outer region in the porous wall, respectively. Thus, the gradient–porous-wall is called. All pin fins had identical size over the cross section, but the gap distance is smaller in the center region and larger in the outer region. The design ensures small bubbles moving out of the porous wall, automatically.

Imagining a liquid flow is established, when the bottom heating is sufficient high, the bubble nucleation preferably occurs in the porous wall. This is because the porous wall contains larger quantity of nucleation sites, compared with the bare channel. The growing bubble cannot be stably populated in the porous wall. Fig. 1c shows a bubble with one end in a smaller space and the other end in a larger space. The pressure difference to drive the bubble motion from smaller space to larger space is

$$P_1 - P_2 = 4\sigma\left[\frac{1}{w_s} - \frac{1}{w_l}\right] \tag{4}$$

where w_s and w_l are the characteristic sizes for smaller space and larger space, respectively. This capillary effect causes the bubble collection in bare channels. The porous wick contains larger liquid content but the bare channel contains large vapor content. The bubble emission direction depend on the pressures in two neighboring bare channels. The bubble always moves to the lower pressure channel. Later we will show that the bubble emission directions are automatically switched between different bare channels.

Once a bubble jet is collected by a bare channel, the bubble is growing due to the film convective heat transfer mechanism. Fig. 1d shows why the high frequency "eye-blinking" motion of the vapor–liquid interface happens. Two bare channels are marked as channel i and channel $i+1$. Pressures are recorded as P_g and P_f inside and outside of the bubble. The vapor pressure related to the liquid pressure, in the two channels, are written as [2]

$$P_{g,i} - P_{f,i} = m_{e,i}^2\left[\frac{\rho_f - \rho_g}{\rho_f \rho_g}\right]_i \tag{5}$$

$$P_{g,i+1} - P_{f,i+1} = m_{e,i+1}^2\left[\frac{\rho_f - \rho_g}{\rho_f \rho_g}\right]_{i+1} \tag{6}$$

where m_e is the evaporation rate. Assuming saturation vapor: $P_{g,i} = P_{sat}(T_{g,i})$ and $P_{g,i+1} = P_{sat}(T_{g,i+1})$, where T_g is the vapor temperature. The pressure difference across the porous wall is

$$P_{f,i} - P_{f,i+1} = P_{sat}(T_{g,i}) - P_{sat}(T_{g,i+1}) - \left\{m_{e,i}^2\left[\frac{\rho_f - \rho_g}{\rho_f \rho_g}\right]_i - m_{e,i+1}^2\left[\frac{\rho_f - \rho_g}{\rho_f \rho_g}\right]_{i+1}\right\} \tag{7}$$

Assuming vapor as an ideal gas, $P_{sat}(T_g) = \rho_g R T_g$, where R is the gas constant for vapor, Eq. (7) is rewritten as:

$$P_{f,i} - P_{f,i+1} = \rho_g R(T_{g,i} - T_{g,i+1}) - \left\{m_{e,i}^2\left[\frac{\rho_f - \rho_g}{\rho_f \rho_g}\right]_i - m_{e,i+1}^2\left[\frac{\rho_f - \rho_g}{\rho_f \rho_g}\right]_{i+1}\right\} \tag{8}$$

Eq. (8) is the pressure difference to drive liquid flow across the porous wall, yielding mass exchange between two channels. If evaporation is more intensive in channel i, then liquid flow direction is from channel i to channel $i+1$.

Because bubble nucleation appears in the porous wall and the vapor flows towards bare channels automatically, the vapor void fractions in bare channels are significantly larger than those in the porous wall. Thus, it is reasonable to assume the film convective heat transfer mechanism exists in bare channels. Recording α as the heat transfer coefficient and A as the vapor–liquid interface area per unit flow length. The following equation exists

$$qW = \alpha A(T_w - T_g) \tag{9}$$

where q is the heat flux at the bottom wall and W is the bare channel width. We define αA as the film convective heat transfer intensity. The more intensive evaporation yields the bubble expansion and increased αA in channel i than in channel $i+1$. Thus, based on Eq. (9), the temperature difference $T_w - T_g$ is lowered in channel i, having a tendency to cause the bubble contraction in channel i. This is the negative feedback control to suppress the bubble expansion in bare channel, the liquid flow direction is switched to be from channel $i+1$ to channel i. Thus, the "eye-blinking" phenomenon is self-sustained.

4. Experimental details

4.1. Design of the gradient–porous-wall microchannel

Fig. 2a shows the gradient–porous-wall microchannel. The silicon substrate had the overall size of 32 mm in length, 10.5 mm in width and 400 μm in thickness. The etched silicon substrate was bonded with a 7740 glass cover. The chip included the silicon substrate, inlet and outlet rectangular holes for plenums, and a deposited platinum film heater at the bottom wall. A planar coordinate system was established, with the origin point (0,0) located at a corner of microchannels. The X and Y coordinates refer to the horizontal coordinate (flow direction) and longitudinal direction (perpendicular to flow direction), respectively. Fig. 2b shows the cross section of microchannels. The microchannels had a length of 20.0 mm and a total width of 5500 μm. The etched depth was 75 μm. A bare channel and a porous wall had a width of 164 μm and 336 μm, respectively. Each pin fin had a cross section size of 15 μm by 15 μm. The densely and sparsely populated pin fin regions had the fin gaps of 5 μm and 15 μm, respectively. Thus, the gradient–porous-wall is formed. The bare channels are marked as 1–10 (not including the two half bare channels near the side walls, see Fig. 2b). Fig. 2c and d shows the SEM images near the inlet hole region and the microchannel network. The pin fins were arranged with an inclination angle of 45° with respect to the axial flow direction.

The back silicon wall was deposited by a thin platinum film with a thickness of 300 nm. The deposition area was exactly identical to the microchannel area. Two gold pads were populated at the two margins of the platinum area. The thin film was the heater for boiling experiment. The electrical resistance was 64.8 Ω at 24 °C. The heater was driven by a DC (direct current) voltage module.

The porous-wall microchannel heat sink was fabricated by the MEMS (microelectricalmechanicalsystem) technique. The wafer is taken through a photolithography step and a reactive ion-etching (RIE) oxide removal process to mask certain areas on the wafer, which are not to be etched during the deep reactive ion etching (DRIE) process. The wafer is consequently etched in a DRIE process, and silicon is removed from places not protected by the photoresist/oxide mask.

4.2. Experimental setup and procedure

Fig. 3 shows the experimental setup, including four subsystems: a liquid tank, a forced convective loop, a microchannel test section and a measurement system. The acetone flow was driven by a pressurized nitrogen gas pressure. The capillary tube inside which acetone was flowing was immersed in a hot water bath, which was running at a constant temperature. Two porous filters, one with

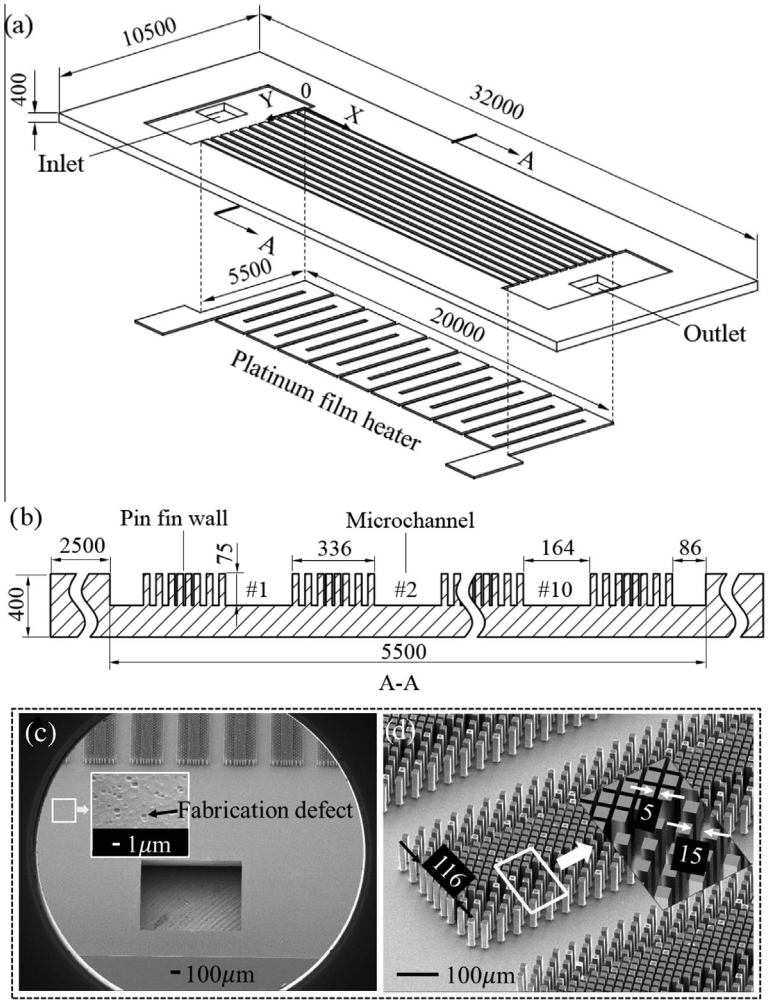

Fig. 2. The gradient–porous-wall microchannels ((a) for 3D drawing, (b) for cross section view of the microchannels, (c) for SEM near the microchannel entrance hole, (d) for SEM showing the gradient–porous-wall and bare channels).

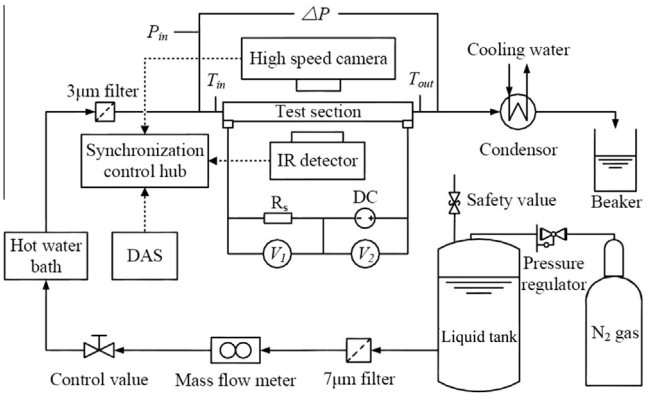

Fig. 3. The experimental setup.

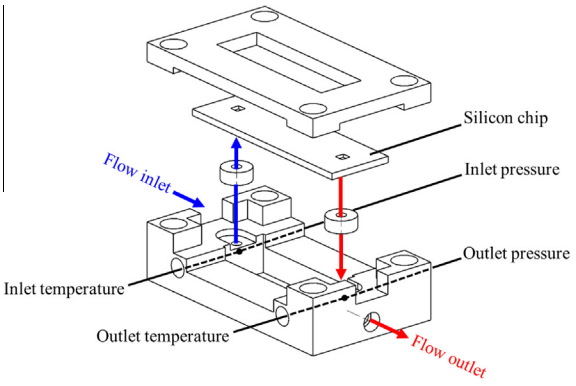

Fig. 4. The housing of the silicon chip.

5–10 μm and the other with 2–5 μm pore size, were arranged in the loop to prevent solid particles from entering the test section.

It is important to remove the non-condensable gas in the acetone liquid. The whole experimental loop was vacuumed before charging acetone liquid. There is an electric heater in the liquid tank bottom (not shown in Fig. 3). Before formal experiment, the acetone was boiled for two hours. When the pressure in the liquid tank reached the set point pressure, the safety valve in the liquid tank top was automatically opened to discharge the vapor. In such a way, the non-condensable gas in liquid was removed. Fig. 4 shows the three-dimensional drawing of the housing of the silicon chip, in which inlet and outlet temperatures and pressures are shown. The flow direction was also demonstrated.

The acetone flow rate was measured by a coriolis mass flow meter (DMF-1-1AB), having an accuracy of 0.5% and a response time of 0.1 s. A pressure transducer (Rosemount 3051) measured

Table 1
The major parameters, instruments and uncertainties.

Parameter	Explanations	Instruments	Uncertainty or relative error
A_{film}	Thin film heating area	Chemical vapor deposition	0.01%
A_c	Effective cross section area of the microchannel	Advanced silicon etch	0.01%
w	Bubble width	Pixel ruler	±5 μm
W	Bare channel width	Physical vapor deposition	0.01%
G	Mass flux	Coriolis mass flow meter (DMF-1-1AB)	0.50%
ΔP	Pressure drop across the microchannel	Pressure transducer (Rosemount-3051)	0.10%
P_{in}	Inlet pressure of the microchannel	Pressure transducer (Rosemount-3051)	0.10%
Q	Total heating power	Voltage module (Yokogawa DL750)	±0.12 W
q	Effective heat flux		1.7–6.0%
$T_{X,Y}(t)$	Wall temperature at the location (X,Y) at time t	IR detector (Infra TecImageIR 5300)	Sensitivity of 0.02 °C, accuracy of 0.2 °C, response time of 1 ms
T_{in}, T_{out}	Inlet and outlet flow temperature	K-type thermocouples	0.2 °C

pressures at the test section inlet, and a differential pressure transducer (Rosemount 3051) measured pressure drops across the test section. The pressure transducers had the accuracy of 0.1% and response time of 0.1 s. The K type thermocouples (Omega) measured fluid temperatures at the test section inlet and outlet. The thermocouples had the accuracy of 0.2 °C and response time of 0.2 s. The recording rates for pressures and temperatures were 500 samples per second. The sampling time was longer than 10 s for each run. The sampling rate and time for all the transducers were identical.

A combined measurement system included a high speed data acquisition system, a high speed camera adapted with a microscope, and a high speed IR (infrared radiator) imaging system. The three equipments were synchronized by a synchronization control hub. During experiments, the data acquisition system and the optical system were in the waiting mode. The synchronization hub sent a signal to trigger functions of these systems. The maximum time difference of the initial function of these systems after they received the triggering signal was less than 1 μs. A computer collected all image files and data.

The high speed data acquisition system (Yokogawa DL750, Japan) collected pressure (voltage signal), fluid temperature and voltage applied on the thin film heater. The sampling rate could be up to 10 MHz for sixteen channels. The sampling rate was 500 Hz in this study.

The IDT Motion pro Y4 (USA) high speed camera system had the spatial resolution of 1280 pixels by 1024 pixels. The maximum recording speed was 58,000 frames per second. The minimum exposure time was 1 μs. In this study, the recording rate of 2500 or 5000 frames per second was used.

This study used an advanced IR image system (Infrared Camera Image IR 5300 Series, Germany) adapted with a micro-lens. The spatial resolution was 320 pixels by 256 pixels. The viewed area was focused on 20,000 μm by 5500 μm. The viewed area was identical to the microchannel area. The microchannel width of 5500 μm corresponds to 25 pixels. Thus, the size resolution was 220 μm. The IR image system had a thermal sensitivity of 0.02 K. The measurement required a careful calibration of the emissivity, depending on the surface topography and wavelengths that are interrogated [27]. A very thin black lacquer was uniformly painted on the thin film heater surface. An emissivity of 0.99 yields good measurement accuracies. The temperature dependence of emissivity can be neglected. The IR image system was calibrated against a set of standard temperatures with an accuracy of 0.2 °C. Table 1 shows the major parameters, instruments and uncertainties. The recording rate of 500 samples per second was used for the IR image system.

The test section is horizontally positioned. The microscope combined with the high speed camera was at the top of the test section to observe flow patterns in microchannels. The IR image system was below the test section to detect the temperature field at the back surface of the silicon chip.

Pure acetone liquid (CH_3COCH_3, molecular weight 58.08, purity >99.5%) was used. It has a saturation temperature of 56.4 °C at atmospheric pressure and is widely used in heat transfer experiments [28]. Other fluids (methanol, ethanol, FC-72, etc), can also be used for boiling experiments [29]. Water is a different coolant in its higher saturation temperature and larger surface tension and latent heat of evaporation, compared with acetone. The physical properties of acetone are taken from Ref. [28].

The net heating power received by microchannels was

$$Q = \varphi(V_2 - V_1)\frac{V_1}{R_s} \tag{10}$$

where $V_2 - V_1$ is the voltage applied on the thin film heater, V_1/R_s is the current flowing through the heater (see Fig. 3), φ is the thermal efficiency, which is experimentally determined to be 0.94. Before the two-phase experiment, the single-phase liquid flow was established, φ was determined by the energy balance in terms of the measured inlet and outlet temperatures [30], i.e., $\varphi = mC_p(T_{out} - T_{in})/Q_t$, where m is the mass flow rate of liquid acetone, C_p is the specific heat of acetone, Q_t is the heat power recorded by the power meter. Thus, the effective heat flux based on the heater surface area is $q = Q/A_{film}$, where A_{film} is the thin film heater area (20.0 mm length by 5.5 mm width, see Fig. 2a).

An effective across section area of the microchannel network is defined as

$$A_c = \frac{V_{vacuum}}{l_{mc}} \tag{11}$$

where V_{vacuum} is the vacuum volume in the microchannel region excluding all the pin fin volume, l_{mc} is the microchannel length (20.0 mm here). Thus, the mass flux is defined as $G = m/A_c$, where m is the total mass flow rate. It is noted that the previous study such as Kosar and Peles [31] used the uniform pin fin structure. The mass flux was defined as the mass flow rate divided by the minimum cross sectional area corresponding to the narrowed pin fin gaps. The present study used the non-uniform pin fin structure, which is not reported in the previous literature. Here, the mass flux was defined as the mass flow rate divided by the effective cross sectional area, reflecting the flow rate effect. The vapor mass quality at the microchannel exit is calculated as

$$x_{out} = \frac{h_{in} + \frac{Q}{m} - h_{f,sat}}{h_{fg}} \tag{12}$$

where h_{in}, $h_{f,sat}$ and h_{fg} are the inlet liquid enthalpy, saturation liquid enthalpy and latent heat of evaporation defined at the exit pressure.

Table 2
The operation parameters for selected runs.

Run	G (kg/m^2 s)	q (kW/m^2)	T_{in} (°C)	P_{in} (kPa)	ΔP (kPa)	x_{out}	f of density wave (Hz)
1	155	32.90	50.1	24.16	26.38	0.111	8.9
13	154	109.64	50.7	95.58	97.22	0.438	14.1
20	154	167.61	50.0	160.12	162.09	0.681	15.9
35	174	69.64	52.5	56.00	54.87	0.244	13.4
36	187	95.89	51.8	80.42	79.56	0.315	14.4
42	181	179.54	48.5	161.63	161.07	0.610	16.4
48	230	30.24	50.3	26.03	27.92	0.060	9.0
59	234	130.95	50.7	124.53	123.11	0.340	15.0
63	224	177.56	51.2	180.77	184.31	0.493	16.5

Note: the f value in the last column is the predicted density wave oscillation frequency assuming walls without holes.

The experiment covered the following data ranges: T_{in} = 47.2–52.5 °C, ΔT_{sub} = 9.6–41.9 °C, G = 154–276 kg/m^2 s, q = 27.22–227.05 kW/m^2, x_{out} = 0.029–0.783. Totally 75 runs were performed. Table 2 listed parameters for selected runs (not all).

5. Results and discussion

5.1. Ultra-stable wall temperatures

Covering the data ranges (75 runs), all the measured parameters are very stable. Fig. 5 shows P_{in} (inlet pressures), T_{in} (fluid inlet temperatures) and T_{out} (outlet temperatures), $T_{w,ave}$ and T_w (wall temperatures), noting that $T_{w,ave}$ is averaged over the whole heater area (20.0 mm by 5.5 mm) at time t. Fig. 5a and b are for run 1 (x_{out} = 0.111, left column) and run 63 (x_{out} = 0.493, right column),

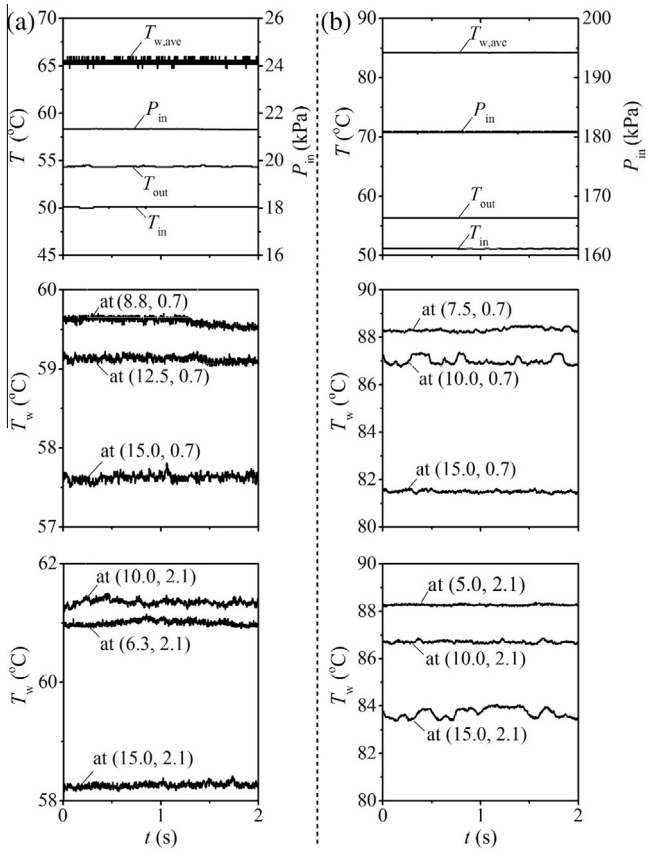

Fig. 5. Various parameters versus time ((a) for run 1 (left column) with G = 155 kg/m^2 s, q = 32.90 kW/m^2, T_{in} = 50.1 °C, x_{out} = 0.111, (b) for run 63 (right column) with G = 224 kg/m^2 s, q = 177.56 kW/m^2, T_{in} = 51.2 °C, x_{out} = 0.493).

respectively. The sampling time covered 2 s. The position of the corresponding wall temperature T_w is identified by the coordinates inside round brackets (X,Y), adopting the coordinate system depicted in Fig. 2a in millimeters. For instance, (8.8,0.7) means X = 8.8 mm and Y = 0.7 mm.

The standard deviation temperature σ quantifies the wall temperatures oscillation degree:

$$\sigma(X,Y) = \sqrt{\frac{1}{n-1}\sum_{i=1}^{n-1}\left(T_{X,Y}(t) - \overline{T}_{X,Y}\right)^2} \tag{13}$$

where $T_{X,Y}(t)$ is the wall temperature at (X,Y) and time t, $\overline{T}_{X,Y}$ is the time averaged temperature over 2.0 s (1000 data with 500 samples per second), n is the number of samples (n = 1000 here). The smaller σ, the more stable wall temperature is. Fig. 6 shows σ for runs 1, 13, 20, 35, 36, 42, 48, 59 and 63, respectively. The operation parameters for these runs are listed in Table 2. The σ values are presented along X at Y = 2.75 mm. The temperature deviations are very small, with the minimum and maximum values of 0.02 °C and 0.18 °C, respectively.

5.2. High frequency "eye-blinking" interface motion

We describe the high frequency "eye-blinking" interface motion in the bare channel width direction. Fig. 7a shows flow pattern near the onset of nucleation boiling (ONB) location for run 1. The visualization region including bare channels #4 and #5 as well as the porous-wall is shown. The red curves are the bubble envelope in the bare channel while the blue arrows show the bubble emission direction. The observation supports the above analysis. The bubble nucleation took place in the porous wall. The vapor is emitted from porous wall to bare channel, either to channel #4, or to channel #5. For instance, the vapor jet flows towards channel #4 at t_1. Then, the bubble is growing and flowing downstream (without flowing upstream), increasing pressure to change bubble emission direction. Thus, the bubble jet flows towards channel #5 at t_1 + 0.8 ms. The vapor jet returns to flow towards channel #4 at t_1 + 2.4 ms. In such a way, the bubble emission direction is periodically switched between two neighboring channels, which is called the "bubble emission switch" phenomenon. The switch time is in the order of ~1 ms, corresponding to the switch frequency of ~1000 Hz. The bubble emission from porous wall to bare channel is based on the surface energy principle (see Eq. (4)). Because the porous wall contains large quantity of nucleation sites, the thermal non-equilibrium between vapor and liquid is weak, which can be verified by the ONB point occurring at the place where the liquid superheating degree is small. For example, the liquid superheating in the visualization region was about 2 °C in Fig. 7a.

We did observe the bubble nucleation in the porous wall region through the microscope with an eye lens of ten times amplification ratio. The images can only be observed by the naked eye but cannot be stored by the computer. However, the vapor ejection direction from the porous wall region to the bare channel region is clearly identified by the high speed camera adapted with the microscope.

Fig. 7b shows flow pattern near the channel exit region. The elongated bubble flow occurs. In contrast to the conventional elongated bubbly flow in microchannels with solid walls, the bubble is not fully confined in the channel width direction. Much attention was paid to the bubble widths, which are periodically changed in ~1 ms timescale. For example, the bubble is fat at t_2, t_2 + 0.4 ms, it is slim at t_2 + 1.2 ms, but it returns to be fat at t_2 + 1.6 ms again (see Fig. 7b).

The bubble confinement ratio is newly defined as

$$\eta = \frac{\text{bubble width}}{\text{bare channel width}} = \frac{w}{W} \tag{14}$$

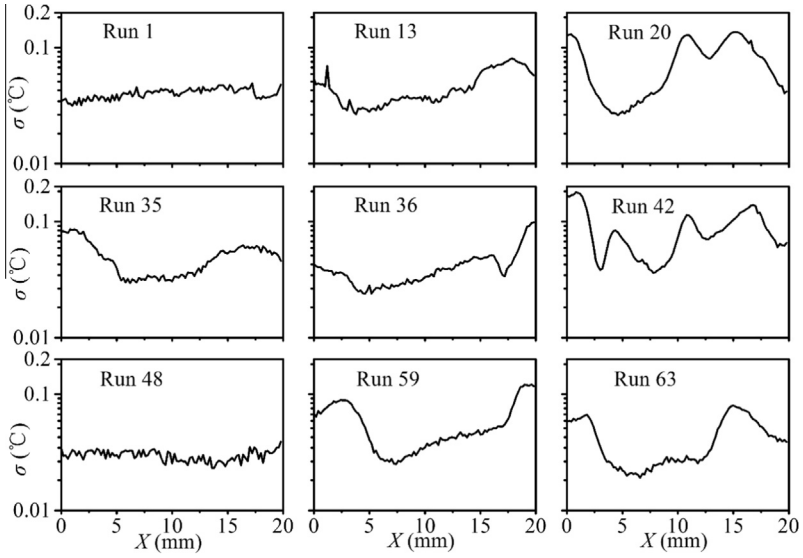

Fig. 6. The standard deviation temperatures (σ) along the flow length at half width of the microfluidic chip for various runs.

The bubble width is obtained by counting the number of pixels in which the bubble is covered. The bare channel width is 164 μm corresponding to 45 pixels. Thus, the size resolution is 3.64 μm/pixel. The bubble width is $w = 3.64\,n_p$, having the unit of micron, where n_p is the number of pixels covered by the bubble width. The accuracy of the bubble width is 3.64 μm, having the relative error of 2.22%. The pixel counting process was performed manually on the computer screen.

The definition of η can be seen in Fig. 8a, where w_i is the bubble width in channel i. The parameter η equals to 1 for elongated bubble in conventional microchannels, but it can be less than 1 in porous-wall microchannels. Transient bubble confinement ratios are shown in Fig. 8b for run 1, see black, red and blue curves for channels #3, #4 and #5, respectively. Power spectrum distribution (*PSD*) analysis was performed. The dominant frequencies are 448.4 Hz, 445.7 Hz and 366.8 Hz for channels #3, #4 and #5, respectively. The dominant frequencies are almost identical between different channels except slightly lower frequency for channel #5. Fig. 8c shows the transient bubble confinement ratios in a narrow time-span (0–10 ms), each displaying quasi-sine function. The bubble confinement ratios are out-of-phase between two neighboring bare channels. When channel i reached maximum $\eta = w/W$, channel $i+1$ reached minimum; when channel i reached minimum $\eta = w/W$, channel $i+1$ reached maximum. Fig. 9 shows the elongated bubble pattern periodically switched between fat bubble and slim bubble in a specific channel, the bubble widths had opposite variation trends between two neighboring channels.

A different case was shown in Figs. 10 and 11 for run 36. Similar phenomenon was found. The w/W curves had almost same dominant frequencies for bare channels #4 (344.4 Hz) and #5 (327.4 Hz). The two curves had opposite variation trends versus time, showing the out-of-phase characteristic. The bubble patterns are switched between fat and slim periodically. The relationships between three channels are seen in Fig. 11. When bubble in channel #4 is fat, bubbles in channels #3 and #5 are slim, under which the bubble in the center channel expels the liquid towards channels #3 and #5. On the contrary, when bubble in channel #4 is slim, bubbles in channels #3 and #5 are fat, under which the center channel receives the liquid from channels #3 and #5. The switch process is self-sustained in ~ms timescale.

The periodical bubble expansion and shrink in bare channels cause liquid mass exchange between neighboring channels across porous-wall. Fig. 12 examines the bubble margins for channels #3–5 (run 1), and for channels #4 and #5 (run 36). Note that for each bare channel, the vertical coordinates of 0 and 1 represent the bare channel margins interfaced with the pin–fin walls. The value of 0.5 represents the bare channel center in the channel width direction. The bubble center (represented by the dashed line) is almost stabilized at the channel center (0.5). The solid curves show the vapor–liquid interface locations, showing the "eye-blinking" motion. Fig. 12a shows that during the period of 2.5–3.0 ms, the bubbles in channels #3 and #5 are expanding but the bubble in channel #4 is shrinking. The overpressure expansion in channels #3 and #5 squeezes liquid from these two channels to channel #4 (see the two solid arrows in Fig. 12a). But the channel #4 behaves the bubble expansion at $t = 4.0$ ms, expelling liquid from channel #4 to channels #3 and #5 (see the open arrow). The "eye-blinking" interface motion periodically changed the mass exchange direction through the porous-wall.

5.3. Density wave propagation over the channel width direction

Porous-wall microchannels overcome shortcomings of conventional microchannels. Because liquid mass exchange can be performed in the channel width direction, the bubble expansion induced over-pressure can be instantaneously transmitted to its neighboring channels. Because liquid film convective heat transfer is related to the vapor–liquid interface area, the expanding bubble causes heat transfer enhancement to lower wall temperatures (see Eqs. (8) and (9)), being the negative feedback mechanism to limit bubble expansion. Thus, the bubble returns to be shrinking. Porous-walls change confined bubble flow to un-confined bubble flow. Bubbles are freely expanding not only along the axial flow direction, but also in the channel width direction, leaving more space for liquid flow rate. Thus, microchannels are never blocked by bubbles.

We identified quasi-uniform vapor–liquid phase distribution between different channels. The situation such as some of channels occupied by liquid but some of channels occupied by vapor, happened in conventional microchannels [30], never occurs in porous-wall microchannels. Strong mixing takes place in porous-wall microchannels, enhancing heat transfer in bare channels and porous walls.

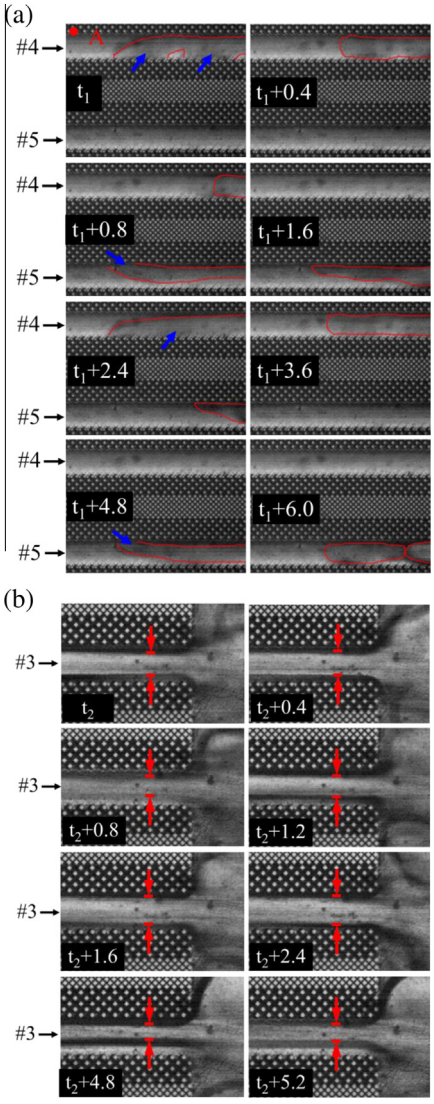

Fig. 7. The bubble emission switch phenomenon near the ONB location (a) and the periodically changed bubble widths near the microchannel exit (b) with A (X = 6.3 mm, Y = 1.4 mm) and run 1 (G = 155 kg/m^2 s, q = 32.90 kW/m^2, T_{in} = 50.1 °C, x_{out} = 0.111).

Physically, the "eye-blinking" interface motion is a density wave oscillation, having much higher frequency than that in conventional microchannels. Let us deal with density wave oscillation in conventional microchannels first. The disturbance of vapor–liquid densities is propagated along axial flow length only. The oscillation frequency is inverse to the fluid residence time τ_r in microchannels: $f \sim 1/\tau_r$ [6]. The whole channel length was divided into a liquid flow length (l_{sp}) and a boiling flow length ($l_{tp} = l_{mc} - l_{sp}$). The fluid residence time in the liquid flow section was $\tau_{sp} = \rho_f l_{sp}/G$, where l_{sp} was

$$l_{sp} = \frac{G\delta_c(h_{f,sat} - h_{in})}{q} \tag{15}$$

where δ_c is the etched channel depth (δ_c = 75 μm here). Now we evaluate the fluid residence time in the two-phase region, noting that x_{out} is predicted by Eq. (12). The average vapor mass quality in the two-phase region was $x_m = 0.5x_{out}$. The slip ratio in the two-phase region, S_{tp}, was the ratio of vapor velocity to liquid velocity [32]:

$$S_{tp} = 0.4 + 0.6\sqrt{\frac{0.4 + \left[\frac{\rho_f}{\rho_g} - 0.4\right]x_m}{0.4 + 0.6x_m}} \tag{16}$$

Thus, α_m (average void fraction), ρ_m (mixture density) and τ_r are as follows [16]:

$$\alpha_m = \frac{1}{1 + \frac{1-x_m}{x_m}\frac{\rho_g}{\rho_f}S_{tp}} \tag{17}$$

$$\rho_m = \alpha_m\rho_g + (1-\alpha_m)\rho_f \tag{18}$$

$$\tau_r = \tau_{sp} + \tau_{tp} = \frac{\rho_f l_{sp}}{G} + \frac{\rho_m(l_c - l_{sp})}{G} \tag{19}$$

The above estimation yields the oscillation frequencies in the range of 8.9–25.5 Hz for the 75 runs (see Table 2), but the low frequency oscillation (~10 Hz) was not detected in this study. The above analysis was based on the density wave propagation along the flow length, characterized by the channel length l_{mc} = 20.0 mm. On the contrary, the "eye-blinking" oscillation had the frequencies in the range of 300–900 Hz, equivalent to 10–100 times of the conventional density wave oscillation frequencies. The porous-wall propagates the density wave in the channel width direction. The "eye-blinking" frequency is scaled by $f \sim v_r/W_{porous}$, where v_r is the radial velocity in the porous wall and W_{porous} is the porous wall width. The "eye-blinking" frequencies being 10–100 times of the axially propagated density wave frequencies, is consistent with the size ratio of the channel length (l_{mc} = 20.0 mm) to the porous wall width (W_{porous} = 336 μm): l_{mc}/W_{porous} = 59.5.

5.4. Wall temperatures stabilized by "eye-blinking" interface motion

A connection between "eye-blinking" interface motion and wall temperatures was established. An "integration parameter model (IPM)" was proposed in Fig. 13. The whole flow length was divided into many subsections, each having a short length. The IPM is based on the ultra-low *Biot* number:

$$Bi = \frac{\text{thermal resistance by boiling heat transfer in microchannels}}{\text{thermal resistance by heat conduction of solid wall}} \tag{20}$$

For boiling heat transfer coefficient of ~10^4 W/m^2 K and thin silicon wall thickness of 325 μm (excluding pin fin thickness), the *Bi* number is ~10^{-2}, at which the solid temperatures in a unit is uniform. The solid material can be treated as a one-dimensional block (such as a solid sphere). Fig. 13a–c shows a unit flow length (including a bare channel and two half porous-walls), the definition of bubble confinement ratio, and the solid sphere. The energy equation is written for the solid sphere

$$m_s C_{p,s}\frac{dT_w}{dt} = Q_h - \alpha A(T_w - T_{sat}) \tag{21}$$

where m_s and $C_{p,s}$ are the mass and specific heat of the solid sphere, respectively, Q_h is the heat source, α is the convective heat transfer coefficient, A is the vapor–liquid interface area in a length l_{unit}, T_{sat} is the saturation temperature ($T_{sat} = T_g$). Q_h is computed as

$$Q_h = q(W + W_{porous})l_{unit} \tag{22}$$

We define αA as the film convective heat transfer intensity. By neglecting the curvature variation of the vapor–liquid interface in channel depth direction, A and αA follow the variation of $\eta = w/W$. The following equation exists

$$[\alpha A](t) = [\alpha A]_{ave}(1 + S_n\sin(2\pi ft)) \tag{23}$$

where the subscript *ave* means the time averaged value, S_n is the non-dimensional oscillation amplitude in the bare channel width direction:

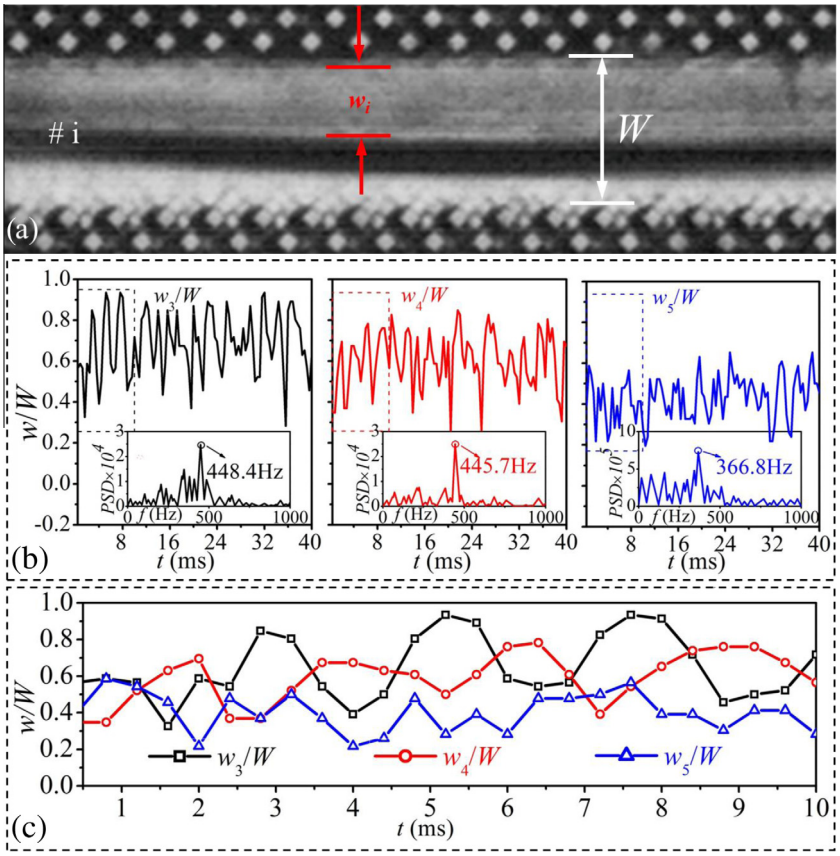

Fig. 8. High frequency "eye-blinking" motion of the vapor–liquid interface (a) definition of bubble confinement ratio, (b) the parameter $\eta = w/W$ versus time, (c) the out-of-phase bubble confinement ratios in three bare channels, run 1 with $G = 155$ kg/m^2 s, $q = 32.90$ kW/m^2, $T_{in} = 50.1$ °C, $x_{out} = 0.111$).

$$S_n = \frac{\left[\frac{w}{W}\right]_{\max} - \left[\frac{w}{W}\right]_{ave}}{\left[\frac{w}{W}\right]_{ave}} \tag{24}$$

Note that at the average sate, the following equation exists:

$$[\alpha A]_{ave} = \frac{Q_h}{(T_{w,ave} - T_{sat})} \tag{25}$$

The solid sphere temperature is solved by combining Eqs. (21)–(25):

$$m_s C_{p,s} \frac{dT_w}{dt} = -Q_h S_n \sin(2\pi f t) \tag{26}$$

We remember that at $t = 0$, $T_w = T_{w,ave}$. T_w has the following expression

$$\begin{aligned} T_w &= T_{w,ave} + \frac{Q_h}{m_s C_{p,s}} \times \frac{S_n}{2\pi f} \times (\cos(2\pi f t) - 1) \\ &= T_{w,ave} + q \times \frac{(W + W_{porous}) l_{unit}}{m_s C_{p,s}} \times \frac{S_n}{2\pi f} \times (\cos(2\pi f t) - 1) \end{aligned} \tag{27}$$

The temperature includes an average term plus an oscillation term. The oscillation term is proportional to q and S_n, but is inversely proportional to the oscillation frequency of bubble confinement ratio, f. The higher the f, the smaller the temperature oscillation amplitude is, yielding ultra-stable wall temperatures. By comparing Eqs. (23) and (27), the phase angle between (αA) and T_w is $3\pi/2$. Wall temperatures are decreased when bubble is expanding, and they are increased when bubble is contracting, accounting for the negative feedback mechanism to eliminate the channel blockage in microchannels.

Two runs are examined. For run 1, we select $l_{unit} = 100$ μm. The related parameters are: $Q_h = 1.65$ mW, $T_{w,ave} = 61.42$ °C, $T_{sat} = 59.11$ °C, $(\alpha A)_{ave} = 7.143 \times 10^{-4}$ W/K, $f = 445.7$ Hz and $S_n = 0.49$. The transient wall temperatures are

$$T_w = 61.41 + 0.01(\cos(2.80t) - 1) \tag{28}$$

Note that the unit of t (time) is millisecond. Eq. (28) indicates the maximum to minimum oscillation amplitude of 0.02 °C for T_w, approaching the standard deviation degree σ of 0.03 °C for run 1 (see Fig. 6). Fig. 13d shows relationships between w/W (measured values), $(\alpha A)/(\alpha A)_{ave}$ (correlated by Eq. (23)) and T_w. The heat transfer intensity αA roughly follows the bubble confinement ratio variations (w/W). The phase angle between αA and T_w is $3\pi/2$, accounting for the negative feedback mechanism to sustain the "eye-blinking" interface oscillation, creating ultra-stable wall temperatures.

Similar analysis was performed for run 36 at $X = 10.0$ mm. T_w is written as

$$T_w = 86.71 + 0.03(\cos(2.16t) - 1) \tag{29}$$

Eq. (29) shows T_w has an oscillation amplitude (maximum to minimum) of 0.06 °C.

5.5. Originality, application and future work of the present paper

The originality of the present work is to propose the gradient–porous-wall microchannels for the improvement of the micro-evaporator performance. The gradient–porous-wall can be made by the micro-pin–fin arrays just like reported in this paper. Or, it can be made by sintering metallic particles to separate neighboring

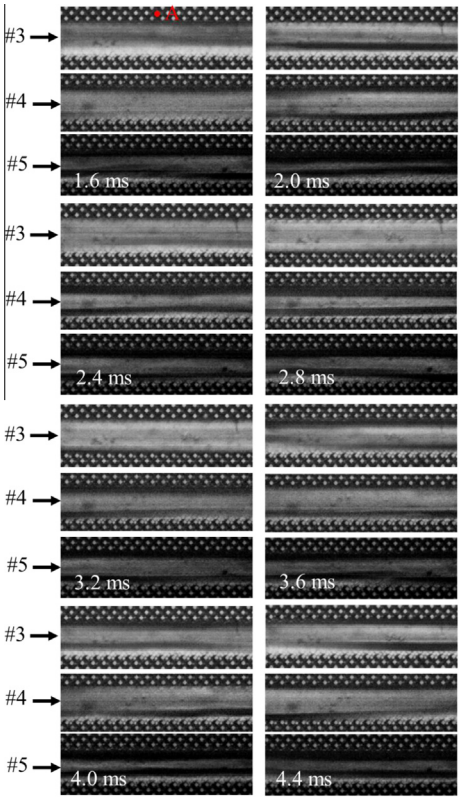

Fig. 9. Images showing the "eye-blinking" motion of the vapor–liquid interfaces, (*A* (10.0 mm, 1.4 mm), run 1 with $G = 155$ kg/m^2 s, $q = 32.90$ kW/m^2, $T_{in} = 50.1$ °C, $x_{out} = 0.111$).

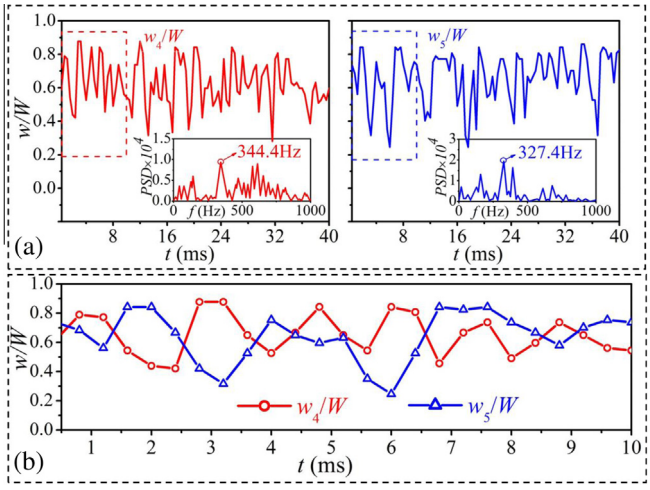

Fig. 10. High frequency "eye-blinking" motion of the vapor–liquid interface (a) the parameter η versus time, (b) the out-of-phase bubble confinement ratios in two bare channels, run 36 with $G = 187$ kg/m^2 s, $q = 95.89$ kW/m^2, $T_{in} = 51.8$ °C, $x_{out} = 0.315$).

channels. The bubble nucleation preferably happens in the porous wall, due to the fact that the porous wall has many nucleation sites. The generated vapor automatically ejects into the bare channels due to the surface tension force driving mechanism.

The porous-wall microchannels change a confined bubble flow to an un-confined bubble flow. This is important because the un-confined bubble flow leaves more space for liquid flow. Thus, the

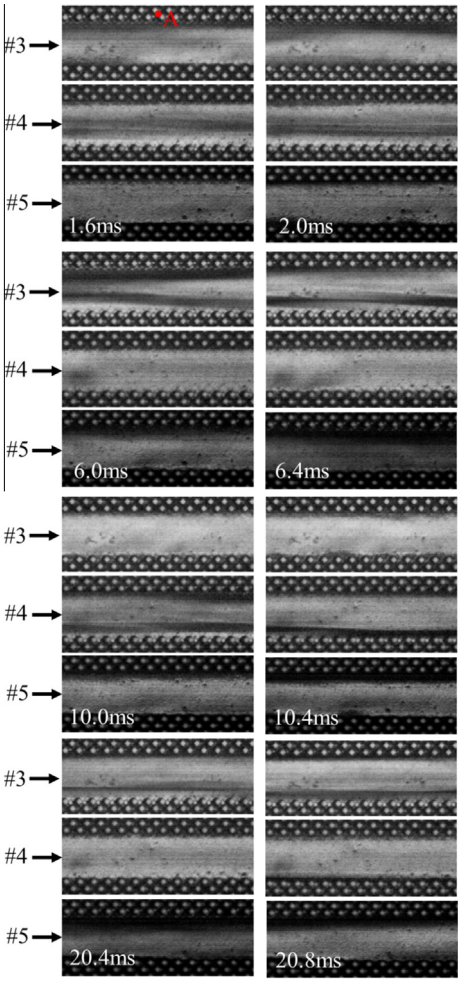

Fig. 11. Images showing the "eye-blinking" motion of the vapor–liquid interfaces, *A* (10.0 mm, 1.4 mm), (run 36 with $G = 187$ kg/m^2 s, $q = 95.89$ kW/m^2, $T_{in} = 51.8$ °C, $x_{out} = 0.315$).

channel blockage and uneven flow distribution can be removed. The bubble confinement ratio is defined as the bubble width relative to the bare channel width, for the first time. It can be less than 1.0. The porous wall increases the liquid mass exchange along the whole flow length, thus it can balance pressure variations between different channels. The bubble confinement ratios are changed in a sine function versus time at high frequencies. The vapor–liquid interface oscillations are always out-of-phase in neighboring bare channels. Further, we identified that the high frequency vapor–liquid interface oscillation is a kind of density wave oscillation. In contrast to the conventional density wave oscillation, the present density wave oscillation propagates in the channel width direction. The smaller porous wall width compared with the channel length is the reason of the high frequency oscillation. Finally, we confirm that the wall temperature oscillation amplitude is inversely proportional to the interface oscillation frequency. The wall temperatures can be kept in an ultra-stable way.

The present finding is useful for microchannel applications. Recently, microchannel heat exchangers can find applications in heat pumps [33], microreactors for methanol steam reforming [34], and miniature compression refrigerator [35], etc. For all these applications, flow and thermal stabilities are important issues that should be solved.

Future work should be continued on geometry optimization of the porous-wall microchannels. Experiments are expected to be

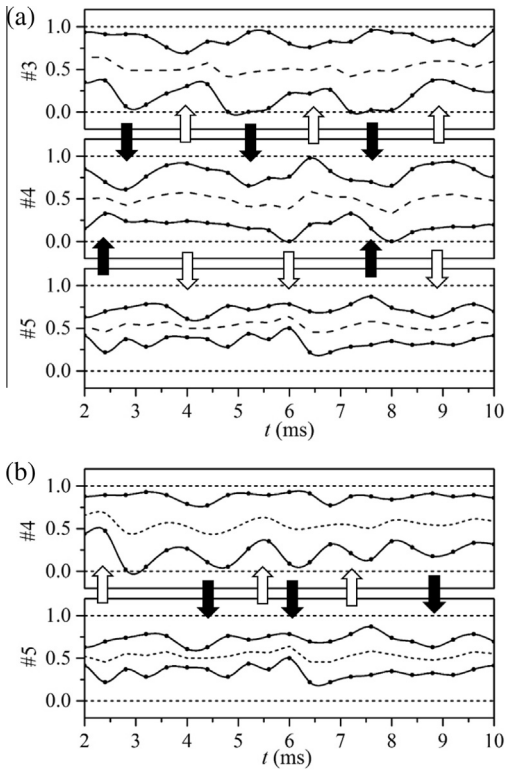

Fig. 12. Elongated bubble interface variation versus time ((a) showing three bare channels for run 1, (b) showing two bare channels for run 36, the arrow showing the liquid flow direction across the porous wall, the axial location is at the half microchannel length X = 10.0 mm).

conducted using different working fluids. Besides, numerical/theoretical work should be done to enhance the understanding of the two-phase flow and heat transfer in porous-wall microchannels.

6. Conclusions

Conventional microchannels have distinct shortcomings. Solid walls prevent fluid exchange along the flow length. Bubble confinement effect leaves small corner region for liquid flow rate, causing channel blockage and non-uniform phase distribution between different channels. Various flow instabilities appear to yield apparent wall temperature oscillations.

The gradient–porous-wall microchannels were proposed. The porous walls contain large quantity of nucleation sites. Vapor generated in the porous wall flows towards bare channels due to the surface tension force driving mechanism. Vapor flow direction is periodically switched between neighboring channels, called the "bubble emission switch" phenomenon.

The porous-walls change confined bubble flow to un-confined bubble flow. Bubble confinement ratio is newly defined, which can be less than 1.0. Bare channels possess fat and slim bubble periodically, in ~ms timescale. Bubble confinement ratios display sine function, and out-of-phase characteristic between two neighboring bare channels, causing the "eye-blinking interface motion". Porous-wall microchannels eliminate channel blockage and non-uniform fluid distribution between different channels.

The "eye-blinking interface motion" is a density wave oscillation, but propagates in the channel width direction. Because the porous-wall width can be much smaller than the channel length, the "eye-blinking" frequencies can be 10–100 times higher than the density wave oscillation frequency characterized by the channel length.

A simple but effective integration parameter model establishes a connection between the "eye-blinking" interface motion and wall temperatures. The model assumes the convective heat transfer intensity in bare channels following the variation of bubble confinement ratios. Wall temperature oscillation amplitude is inversely proportional to the "eye-blinking" frequency. The phase angle between wall temperatures and bubble confinement ratios are $3\pi/2$, being the negative feedback mechanism to inhibit wall temperature oscillations.

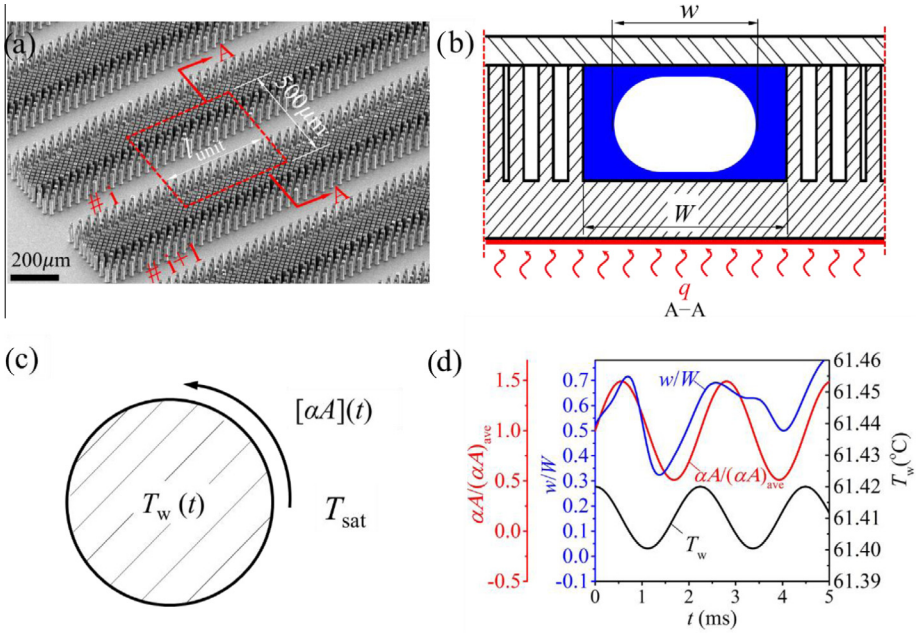

Fig. 13. The "integration parameter model" showing connection between high frequency "eye-blinking" interface motion and wall temperature oscillations ((a) showing a unit for computation, (b) for definition of bubble confinement ratio, (c) showing the "integration parameter model", and (d) showing convective heat transfer intensities and wall temperatures versus time).

Acknowledgements

This paper was supported by the National Natural Science Foundation of China – China (51436004) and the International Cooperation Project of NSFC (51210011).

References

[1] M. Ledinegg, Instability of flow during natural and forced circulation, Die Warme 61 (8) (1938) 891–898.
[2] L. Tadrist, Review on two-phase flow instabilities in narrow spaces, Int. J. Heat Fluid Flow 28 (1) (2007) 54–62.
[3] L.C. Ruspini, C.P. Marcel, A. Clausse, Two-phase flow instabilities: a review, Int. J. Heat Mass Transfer 71 (2014) 521–548.
[4] A.H. Stenning, Instabilities in the flow of a boiling liquid, J. Fluids Eng. ASME 86 (2) (1964) 213–217.
[5] T.N. Veziroglu, A.H. Stenning, "Density-Wave" Oscillations in Boiling Freon-11 Flow, 1966.
[6] K. Fukuda, T. Kobori, Classification of two-phase flow instability by density wave oscillation model, J. Nucl. Sci. Technol. 16 (2) (1979) 95–108.
[7] H.Y. Wu, P. Cheng, Boiling instability in parallel silicon microchannels at different heat flux, Int. J. Heat Mass Transfer 47 (17) (2004) 3631–3641.
[8] J.L. Xu, J.J. Zhou, Y.H. Gan, Static and dynamic flow instability of a parallel microchannel heat sink at high heat fluxes, Energy Convers. Manage. 46 (2) (2005) 313–334.
[9] D. Bogojevic, K. Sefiane, A.J. Walton, H. Lin, G. Cummins, Two-phase flow instabilities in a silicon microchannels heat sink, Int. J. Heat Fluid Flow 30 (5) (2009) 854–867.
[10] J.R. Thome, Fundamentals of boiling and two-phase flows in microchannels, Int. Heat Transfer Conf. 13 (2006).
[11] G. Hetsroni, A. Mosyak, E. Pogrebnyak, Z. Segal, Explosive boiling of water in parallel micro-channels, Int. J. Multiphase Flow 31 (4) (2005) 371–392.
[12] F. Yang, X. Dai, C. Li, High frequency microbubble-switched oscillations modulated by microfluidic transistors, Appl. Phys. Lett. 101 (7) (2012) 073509.
[13] M.Q. Jiang, Y.P. Wei, G. Wilde, L.H. Dai, Explosive boiling of a metallic glass superheated by nanosecond pulse laser ablation, Appl. Phys. Lett. 106 (2) (2015) 021904.
[14] G. Paul, I. Manna, P.K. Das, Formation, growth, and eruption cycle of vapor domes beneath a liquid puddle during Leidenfrost phenomena, Appl. Phys. Lett. 103 (8) (2013) 084101.
[15] D.X. Deng, W. Wan, H.R. Shao, Y. Tang, J.Y. Feng, J. Zeng, Effects of operation parameters on flow boiling characteristics of heat sink cooling systems with reentrant porous microchannels, Energy Convers. Manage. 96 (2015) 340–351.
[16] Z. Lyu, J.L. Xu, X.J. Yu, W. Jin, W. Zhang, Wavelet decomposition method decoupled boiling/evaporation oscillation mechanisms over two to three timescales: a study for a microchannel with pin fin structure, Int. J. Multiphase Flow 72 (2015) 53–72.
[17] D.S. Yoon, Y.S. Lee, Y. Lee, H.J. Cho, S.W. Sung, K.W. Oh, et al., Precise temperature control and rapid thermal cycling in a micromachined DNA polymerase chain reaction chip, J. Micromech. Microeng. 12 (6) (2002) 813–823.
[18] B.W. Shu, C.S. Zhang, D. Xing, A handheld flow genetic analysis system (FGAS): towards rapid, sensitive, quantitative and multiplex molecular diagnosis at the point-of-care level, Lab Chip 15 (12) (2015) 2597–2605.
[19] P. Neuzil, L. Novak, J. Pipper, S. Lee, L.F.P. Ng, C.Y. Zhang, Rapid detection of viral RNA by a pocket-size real-time PCR system, Lab Chip 10 (19) (2010) 2632–2634.
[20] G.D. Wang, P. Cheng, A.E. Bergles, Effects of inlet/outlet configurations on flow boiling instability in parallel microchannels, Int. J. Heat Mass Transfer 51 (9) (2008) 2267–2281.
[21] S.G. Kandlikar, W.K. Kuan, D.A. Willistein, J. Borrelli, Stabilization of flow boiling in microchannels using pressure drop elements and fabricated nucleation sites, J. Heat Transfer 128 (4) (2006) 389–396.
[22] J.L. Xu, G.H. Liu, W. Zhang, Q. Li, B. Wang, Seed bubbles stabilize flow and heat transfer in parallel microchannels, Int. J. Multiphase Flow 35 (8) (2009) 773–790.
[23] Y. Taitel, D. Barnea, Transient solution for flow of evaporating fluid in parallel pipes using analysis based on flow patterns, Int. J. Multiphase Flow 37 (5) (2011) 469–474.
[24] S.G. Kandlikar, Heat transfer mechanisms during flow boiling in microchannels, in: ASME 2003 1st International Conference on Microchannels and Minichannels, American Society of Mechanical Engineers, 2003.
[25] C.W. Wong, T.S. Zhao, Q. Ye, J.G. Liu, Transient capillary blocking in the flow field of a micro-DMFC and its effect on cell performance, J. Electrochem. Soc. 152 (8) (2005) A1600–A1605.
[26] Y.P. Peles, L.P. Yarin, G. Hetsroni, Steady and unsteady flow in a heated capillary, Int. J. Multiphase Flow 27 (4) (2001) 577–598.
[27] J.L. Xu, S. Shen, Y.H. Gan, Y.X. Li, W. Zhang, Q.C. Su, Transient flow pattern based microscale boiling heat transfer mechanisms, J. Micromech. Microeng. 15 (6) (2005) 1344–1361.
[28] J.L. Xu, Y.H. Gan, D.C. Zhang, X.H. Li, Microscale boiling heat transfer in a micro-timescale at high heat fluxes, J. Micromech. Microeng. 15 (2) (2005) 362–376.
[29] G. Ribatski, A critical overview on the recent literature concerning flow boiling and two-phase flows inside micro-scale channels, Exp. Heat Transfer 26 (2–3) (2013) 198–246.
[30] G. Hetsroni, A. Mosyak, Z. Segal, E. Pogrebnyak, Two-phase flow patterns in parallel micro-channels, Int. J. Multiphase Flow 29 (3) (2003) 341–360.
[31] A. Kosar, Y. Peles, Boiling heat transfer in a hydrofoil-based micro pin fin heat sink, Int. J. Heat Mass Transfer 50 (2007) 1018–1034.
[32] S.L. Smith, Void fractions in two-phase flow: a correlation based upon an equal velocity head model, Proc. Inst. Mech. Eng. 184 (1) (1969) 647–664.
[33] B. Xu, Q. Han, J.P. Chen, F. Li, N.J. Wang, D. Li, et al., Experimental investigation of frost and defrost performance of microchannel heat exchangers for heat pump systems, Appl. Energy 103 (2013) 180–188.
[34] D.H. Zeng, M.Q. Pan, L.M. Wang, Y. Tang, Fabrication and characteristics of cube-post microreactors for methanol steam reforming, Appl. Energy 91 (1) (2012) 208–213.
[35] W.X. Yuan, B. Yang, Y.F. Yang, K.X. Ren, J. Xu, Y.B. Liao, Development and experimental study of the characteristics of a prototype miniature vapor compression refrigerator, Appl. Energy 143 (2015) 47–57.